ADVANCED ENERGY & SUSTAINABILITY RESEARCH
www.advenergysustres.com

Oriented for Efficiency: Textured Se Thin Films Fabricated by Vapor Transport Deposition for Emerging Photovoltaic Applications

Ivan Caño, Arnau Torrens, Oriol Segura-Blanch, Edoardo Maggi, Alex Jiménez-Arguijo, Outman El Khouja, Alejandro Navarro-Güell, David Rovira, Andrea Aroldi, José-Miguel Asensi, Xavier Alcobé, Cristina Puigjaner, Rene Schwiddessen, Susan Schorr, Alejandro Pérez-Rodriguez, Diouldé Sylla, Zacharie Jehl, Edgardo Saucedo, and Marcel Placidi*

This work presents a low-temperature vapor transport deposition method to synthesize Se thin films, enabling a precise control over thickness and crystallographic texture. Using a combinatorial synthesis approach, the authors demonstrate a direct correlation between annealing temperature and preferred crystalline orientation, which significantly influences device performance. Films with a strong vertical alignment exhibit reduced Urbach energy and subgap absorption, as well as enhanced optoelectronic properties, resulting in power conversion efficiencies exceeding 4% under AM1.5 G, and up to 10% under indoor illumination, with an excellent fill factor stability and reduced recombination losses. This study highlights the critical role of texture control in determining the optoelectronic quality of anisotropic chalcogenide solar cells and provides an effective strategy for tuning the morphology, crystalline orientation, and optical characteristics of Se thin films.

1. Introduction

Long before modern photovoltaics, selenium was the harbinger of what was to come. In 1876, British physicist William G. Adams and his disciple Richard E. Day demonstrated that illuminating a selenium cylinder connected to Pt wires generated an electric current. In their own words, "*under the action of light a difference of potential [was] developed [...]. The current was produced suddenly on exposure.*" This experiment marked the first documented observation of the photovoltaic effect in a solid-state system.[1] However, the historical connection between Se and photovoltaics (PV) extends beyond Adams and Day's ground-breaking discovery. In 1883, American inventor Charles E. Fritts built the first solar cell in history using a Se thin film compressed between metal plates, achieving an energy conversion efficiency of ≈1%.[2] While Fritts' work reflected the ingenuity and exploratory spirit of 19th-century science, research into solar energy remained largely dormant for the next seven decades. This changed in 1954, when Daryl M. Chapin, Calvin S. Fuller, and Gerald L. Pearson developed the earliest c-Si solar cells with an efficiency of 6%,[3] opening the door to harnessing the Sun's energy for electricity generation on a human societal scale for the first time.

I. Caño, A. Torrens, O. Segura-Blanch, E. Maggi, A. Jiménez-Arguijo, O. El Khouja, A. Navarro-Güell, D. Rovira, A. Aroldi, Z. Jehl, E. Saucedo, M. Placidi
Electronic Engineering Department
Photovoltaic Lab – Micro and Nano Technologies Group (MNT)
Universitat Politècnica de Catalunya (UPC)
EEBE
Av Eduard Maristany 10-14, 08019 Barcelona, Spain
E-mail: ivan.cano.prades@upc.edu

The ORCID identification number(s) for the author(s) of this article can be found under https://doi.org/10.1002/aesr.202500189.

DOI: 10.1002/aesr.202500189

I. Caño, A. Torrens, O. Segura-Blanch, E. Maggi, A. Jiménez-Arguijo, O. El Khouja, A. Navarro-Güell, D. Rovira, A. Aroldi, Z. Jehl, E. Saucedo, M. Placidi
Barcelona Centre for Multiscale Science & Engineering
Universitat Politècnica de Catalunya (UPC)
Av Eduard Maristany 10-14, 08019 Barcelona, Spain

E. Maggi
Chemical Engineering Department
Universitat Politècnica de Catalunya (UPC)
Nanoengineering of Materials Applied to Energy (NEMEN)
Institute of Energy Technologies
EEBE
Av Eduard Maristany 10-14, 08019 Barcelona, Spain

J.-M. Asensi
Applied Physics Department
Universitat de Barcelona (UB)
C. Martí I Franquès 1, 08028 Barcelona, Spain

Following this breakthrough, the efficiency of Si-based solar cells steadily increased, driven in large part by the demands of the space age, as exemplified by the launch of the solar-powered satellite *Vanguard 1* only in 1958. Meanwhile, selenium became relegated to the status of a historical curiosity or, at best, a niche research material. From 1985, Se-based solar cell efficiencies plateaued at around 5% for over three decades.[4–6]

However, around the turn of the millennium, and particularly from the 2010s onwards, Se has started to re-emerge as a material of interest in photovoltaic (PV) research, along with other wide-bandgap materials. The continued expansion of photovoltaics into emerging, nontraditional markets has created a demand for materials and device architectures tailored to the specific requirements of these new applications. These include features such as long-term stability, environmental sustainability, and low-temperature processing. Furthermore, emerging applications such as indoor photovoltaics (IPV) are gaining significant momentum as promising novel directions in solar energy research. Indeed, driven by the rapid growth of Internet-of-Things (IoT) devices, and other low-power electronics, there is a growing demand for reliable energy harvesting solutions that operate efficiently under ambient indoor lighting. Hence, IPV systems, which convert artificial light into electrical energy, represent a viable pathway to sustainably power these devices. In this context, PV materials with wider bandgaps are particularly advantageous, as they align more effectively with the spectral characteristics of indoor light sources, and can operate efficiently under low illumination conditions.[7] Remarkably, the wide bandgap of Se (≈1.9 eV), makes it particularly well-suited for IPV applications, yielding a theoretical Shockley–Queisser limit of around 55% under indoor conditions.[6,8] In addition to its favorable optoelectronic properties, Se is a stable and low-toxic material, with a crystallization temperature of ≈200 °C. Certainly, these characteristics place Se as a strong candidate for next-generation PV technologies, particularly in the context of the expanding IoT landscape.

Despite being composed of a single element, selenium exhibits significant structural complexity, as it is capable of forming various polymorphs, including trigonal and several monoclinic phases. The most thermodynamically stable and widely reported phase is the trigonal selenium (t-Se). Interestingly, this phase features a unique anisotropic, quasi-1D crystal structure, based on molecular Se_n atom ribbons covalently bonded along a single crystallographic direction (typically described as the [00 L] direction). while these chains are held together through weaker Van der Waals interactions.[9] Such structural anisotropy is characteristic of other low-dimensional chalcogenide materials, including Sb_2Se_3 and SbSeI, which have shown improved optoelectronic performance when aligned along their covalently bonded axes.[10–13] In the case of t-Se, first-principles calculations have confirmed that electron mobility is significantly higher along the covalently bonded ribbon direction (26.5 $cm^2 V^{-1} s^{-1}$) compared to that of the interchain directions (7.4 $cm^2 V^{-1} s^{-1}$).[14] This correlation between structural and transport anisotropy underscores the importance of achieving a preferred (00 L) crystallographic orientation to enhance solar cell performance. The quasi-1D nature of t-Se has been recently explored in the context of photovoltaic device engineering, contributing to the latest efficiency milestones: 8.1% under standard AM1.5 G illumination, and over 26% under indoor lighting conditions.[14–17]

To date, Se film fabrication has predominantly relied on a two-step process: thermal evaporation of Se, followed by annealing at elevated temperature (typically ≈200 °C) on a hot plate or furnace. This method effectively produces smooth, uniform films with precise thickness control, enabling deposition of layers as thin as 100 nm.[18] However, due to the weak interaction and near-zero bonding energy between Se and TiO_2, annealing at 200 °C is insufficient to form Se—O bonds.[8] Instead, Van der Waals interactions dominate, resulting in Se ribbons lying flat on the substrate, a configuration that hinders efficient carrier transport. Notably, Ding Jiang Xue et al.[14] demonstrated that substrate heating during deposition can generate reactive Se_2 species, facilitating Se—O bond formation at the Se/TiO_2 interface and promoting vertical growth along the *c*-axis, corresponding to the covalently bonded helical chains. Despite these insights, a systematic study of how deposition temperature influences Se crystallization and texturing is still lacking, and the current methodology typically requires a separate annealing step for crystallization. To address this gap, we propose a combinatorial approach involving a temperature gradient across a series of samples. This strategy enables a systematic, self-consistent study of the relationship between deposition temperature, crystallographic texture, and optoelectronic properties.

In this work, we present a novel process for the fabrication of Se solar cells using vapor transport deposition (VTD).[19,20] This is one of the first implementations of this low-cost, low-temperature, single-step method for Se-based PV devices.[21] In this approach, Se is evaporated at ≈200 °C in a tubular furnace under argon flow, depositing, and crystallizing in situ onto substrates placed at various positions along the tube. Notably, these substrates can be independently subjected to distinct temperatures depending on the furnace configuration. This methodology enables the direct formation of highly crystalline and uniform Se thin films using a single processing step, not requiring any recrystallization on hot-plate or furnace. Remarkably, our process allows Se fabrication at exceptionally low temperatures, with the best-performing devices synthesized at just over 100 °C (likely the lowest temperature reported to date for Se solar cell production); this makes the technique particularly appealing for applications involving temperature-sensitive or flexible substrates, such as polymers. Furthermore, the VTD method

X. Alcobé, C. Puigjaner
Scientific and Technological Centers (CCiTUB)
Universitat de Barcelona (UB)
C. Lluís Solé i Sabaris 1-3, 08028 Barcelona, Spain

R. Schwiddessen, S. Schorr
Department Structure and Dynamics of Energy Materials
Helmholtz-Zentrum Berlin für Materialien und Energie, Hahn-Meitner-Platz 1
14109 Berlin, Germany

S. Schorr
Institute of Geological Sciences
Freie Universität Berlin
Malteserstr. 74–100, 12249 Berlin, Germany

A. Pérez-Rodriguez, D. Sylla, M. Placidi
Solar Energy Materials and Systems Group
Institut de Recerca en Energia de Catalunya (IREC)
Jardins de les Dones de Negre, 1, 08930 Sant Adrià del Besòs, Spain

provides a uniquely suited platform for combinatorial studies by enabling spatially resolved thermal gradients across a single substrate batch. By using a furnace with independently controlled heating zones, substrates can experience distinct thermal environments within a single run; something difficult to achieve with other methods. This approach allows systematic investigation of how synthesis temperature influences structural, optical, and optoelectronic properties of Se films, all while maintaining consistent substrate, chemical precursor, and annealing conditions. Our findings reveal a clear correlation between substrate temperatures and crystalline orientation: that is, vertical alignment along the *c*-axis is favored at a higher temperature (110–120 °C), while lower temperature promotes horizontal growth. Importantly, this structural anisotropy translates into device performance, with solar cells exhibiting efficiencies exceeding 4% when the optimized (00 L) orientation and large grain sizes are achieved. Under indoor illumination, efficiencies of up to 10% have been obtained, underscoring the potential of this material and methodology for IPV applications.

2. Experimental Section

Se thin films were fabricated by a novel VTD, which allowed low-temperature processing, while also offering a versatile platform for combinatorial studies by enabling spatially resolved variations in the thermal processing.

2.1. Device Fabrication

From the substrate (FTO)-coated glass substrates (TEC 15 ≈13 Ω/sq, Sigma-Aldrich) were cleaned by ultrasonication with soap (Liquinox, Alconox), 2-propanol, and Milli-Q water. 30 nm compact TiO_2 layer was deposited by spray pyrolysis at 500 °C, using a precursor solution of Titanium(IV) di-isopropoxide bis(acetylacetonate) (Sigma–Aldrich, 75%) diluted in absolute ethanol with a volume ratio of 1:19. Tellurium (Sigma–Aldrich, 99%) was deposited by thermal evaporation (base pressure $P < 10^{-7}$ mbar) at a rate of 0.1 nm s^{-1} during ≈40 s.[22] Then, Se thin films were deposited via VTD using a tubular furnace. A series of 1×5 cm substrates were placed sequentially along the length of the tube, forming a continuous array of samples, see **Figure 1** for the experimental layout. The deposition was carried out using a three-zone furnace, with each zone independently monitored and controlled. Se pellets were placed on a glass holder positioned in zone T1, which was heated to 200 °C at a ramp rate of 20 °C·min^{-1}. Samples were positioned downstream, between zones T2 and T3, both of which remained unheated throughout the process. An Ar flow was used as the carrier gas, maintained at a pressure of 1.5 mbar. Although zones T2 and T3 were not actively heated, their temperature gradually increased during the annealing process due to thermal inertia from zone T1. The temperature profile along the tube exhibited an exponential decay with increasing distance from Se source. In the specific furnace used for this study, when T1 reached 200 °C, the temperatures of zones T2 and T3 stabilized at ≈60 and 45 °C, respectively. Multiple sample series were prepared by interrupting the process once zone T2 reached different final temperatures. In this article, the authors focused exclusively on the best-performing set of samples, corresponding to conditions where T2 reached 125 °C and T3 reached 100 °C, with total annealing duration of 45 min. Finally, MoO_3 (99.99%, Sigma–Aldrich) and Au (99.99%, Neyco) were deposited by thermal evaporation for solar cell characterization, see Figure 1 (right panel) for the device architecture schematic. To define the individual cells, gold was deposited through a patterned mask with round openings, each with an active area of 0.07 cm^2. The thicknesses of the Se films along the tube were measured by X-ray fluorescence (XRF), see Figure 1 (left panel). We note that the thickness increases rapidly from 600 nm to 1000 nm at the relative position of 20 cm with respect to the Se

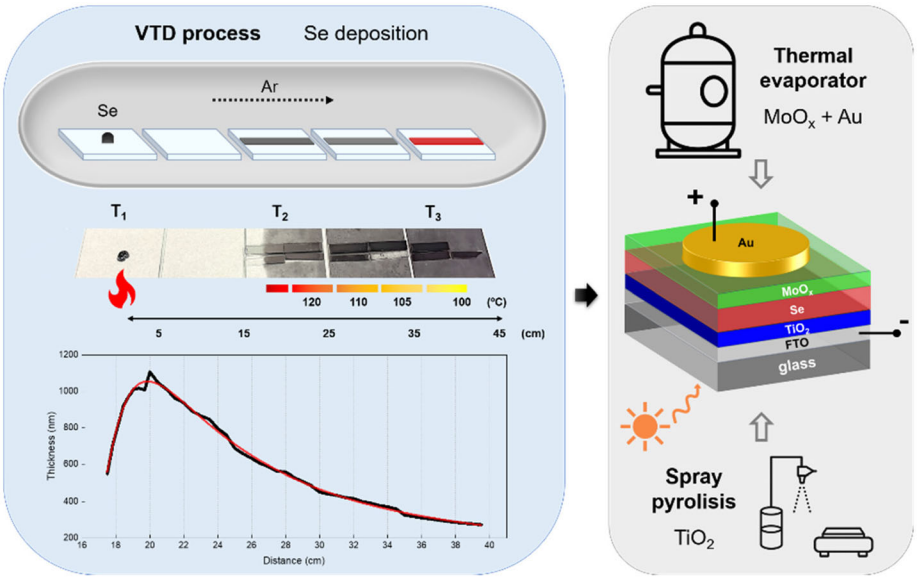

Figure 1. Experimental outline of the VTD process (left panel) and schematic of device superstrate architecture (right). Image includes a photograph of the as-grown Se samples after the annealing, and a plot of thickness (nm) as a function of distance with respect to the Se source.

source (120 °C), indicating the effect of Se re-evaporation at the samples closer to the source, then decreasing slowly as the samples are located farther from the source.

2.2. Film Characterization

XRF spectra were measured with a Fischerscope X-ray XDAL instrument. X-ray diffraction (XRD) data was obtained with PANalytical X'Pert PRO MPD diffractometer in a Bragg–Brentano geometry, using a Cu tube operating at 45 kV and 40 mA, and a solid-state strip 1D PIXcel detector. High statistics, full angular range Cu $K\alpha_{1+2}$ $\theta/2\theta$ scans were obtained with the following parameters: 2θ–θ scans from 4 to 145°, step size of 0.026°, measuring time per step of 200 s (PIXcel^{1D} active length 3.347°), three consecutive repeated scans, and total measuring time per sample of 3.6 h. Pattern matching refinement by the LeBail method was performed using the FullProf software suite.[23] Texture analysis was performed with PANalytical MRD X-ray diffractometer equipped with a Eulerian cradle employing two-axis scans along φ and χ in increments of 5° each. The intensity distribution was recorded along full circles ($\varphi = 0°$ to 360°) and at sample tilts χ ranging between 0° and 85°. Scanning electron microscopy (SEM) micrographs were acquired using a Zeiss Series Auriga field-emission microscope, with an acceleration voltage of 5 kV and working distance ranging of 3 mm. Transverse photothermal deflection spectroscopy (PDS) was used to analyze the weak sub-gap absorption. The setup consisted of a 100 W tungsten halogen lamp, a PTI 01-0002 monochromator (two-grating monochromator with spectral range of 400–2000 nm), and Thorlabs MC1000 optical chopper (4 Hz light modulation frequency). A Signal Recovery 7265 lock-in amplifier was connected to a Hamamatsu C10442-02 PSD detector to measure the deflection of the MC6320C laser probe beam (10 mW). For measurements, the samples were located in a quartz cuvette filled with Fluorinert TM FC-40. A personal computer controlled the monochromator, changed the order filters, and stored the PDS signal read from the lock-in amplifier. UV–vis transmission and reflection spectra were measured with a PerkinElmer Lambda 950 UV–vis–NIR spectrometer.

2.3. Solar Cell Characterization

Current–voltage (J–V) measurements were performed in a superstrate configuration using a 28 LED Class AAA solar simulator (G2V Pico), placed in a black box, both for AM1.5 G and indoor measurements. To simulate indoor illumination conditions, spectra corresponding to white LEDs with different color temperatures (ranging from 2700 to 6000 K) were generated by appropriately adjusting the individual LED output.[24] The incident power density was then varied by changing the overall power level (2970 to 7.5 μW cm^{-2}), maintaining the color temperature. See specifics for each indoor lighting conditions in Table S1, Supporting Information.

3. Results and Discussion

This article is structured into three main sections followed by the conclusions. Each section presents and discusses the results obtained from structural, morphology, and optoelectronic characterizations, respectively, with the key findings summarized in the final conclusions.

3.1. Structural Characterization

A series of nine samples was characterized by XRD to investigate the effect of varying synthesis temperatures on crystalline quality and crystallographic texture. Measurements were conducted in Bragg–Brentano geometry, using a θ–2θ scan range from 10° to 140°. Only one crystalline phase is observed in the absorber layer. It is, in principle, compatible with the α-Se structure, hexagonal, space group $P3_12_1$, $Z = 3$. All diffraction patterns were subsequently analyzed using the Le Bail refinement method to extract lattice parameters and peak characteristics, including full width at half maximum (FWHM) and integrated intensity. The resulting diffraction patterns are shown in **Figure 2**a. Major peak contributions FTO and gold contacts (Au) have been excluded from the plots, specifically in the ranges of 33°–40° and 45°–50°. For the complete set of measured and fitted diffractograms, refer to Figure S1, Supporting Information. Additionally, the main Se diffraction peaks are shown separately in Figure 2b, with normalized and adjusted intensities to facilitate comparison. Remarkably, very clear trends can be observed upon visual inspection. Specifically, the Bragg reflections indexed to the (0kl) and (00 L) planes increase in intensity with higher synthesis temperatures (represented by darker red tones), whereas their intensity progressively diminishes at lower annealing temperatures. This behavior suggests a gradual loss of the (003)-preferred orientation (i.e., the (003) lattice plane is preferentially oriented parallel to the film's surface) as the growth temperature decreases. Conversely, peaks indexed to the (h00) planes exhibit the opposite trend, while the 101 reflection becomes dominant in thin films synthesized between 110 and 115 °C. These observations indicate a preferential (00 L) crystallographic texture in films processed between 120 and 125 °C, whereas lower temperatures favor a shift toward a (h00) orientation, resulting in a horizontal orientation of the Se-ribbons. Overall, these findings demonstrate a strong correlation between crystallographic texture and processing temperature.

To validate these observations, texture coefficients (TCs) have been determined. The TCs provide a qualitative, non-absolute metric enabling comparison of crystallographic texture across different thin films. It is derived by normalizing the integral intensities of Bragg peaks against those expected for a randomly oriented powder pattern (see Equation S(1), Supporting Information). A texture coefficient $TC_{hkl,1} > 1$ indicates an enhanced representation of the $(hkl)_1$ crystallographic plane (i.e., a preferential orientation), whereas $TC_{hkl,2} < 1$ suggests underrepresentation of the $(hkl)_2$ plane in the pattern. It has also been suggested that, in multitextured polycrystalline films, crystallographic planes satisfying the condition $k + l \geq 3$ tend to be oriented at larger angles with respect to the substrate surface—these orientations are generally more favorable for efficient charge transport in selenium. Conversely, planes for which $h + k \geq 3$, tend to indicate horizontal growth (parallel to substrate), which is less desirable for photovoltaic performance in this context. Based on these principles, the TCs of the nine Se samples were evaluated. Figure 2c displays

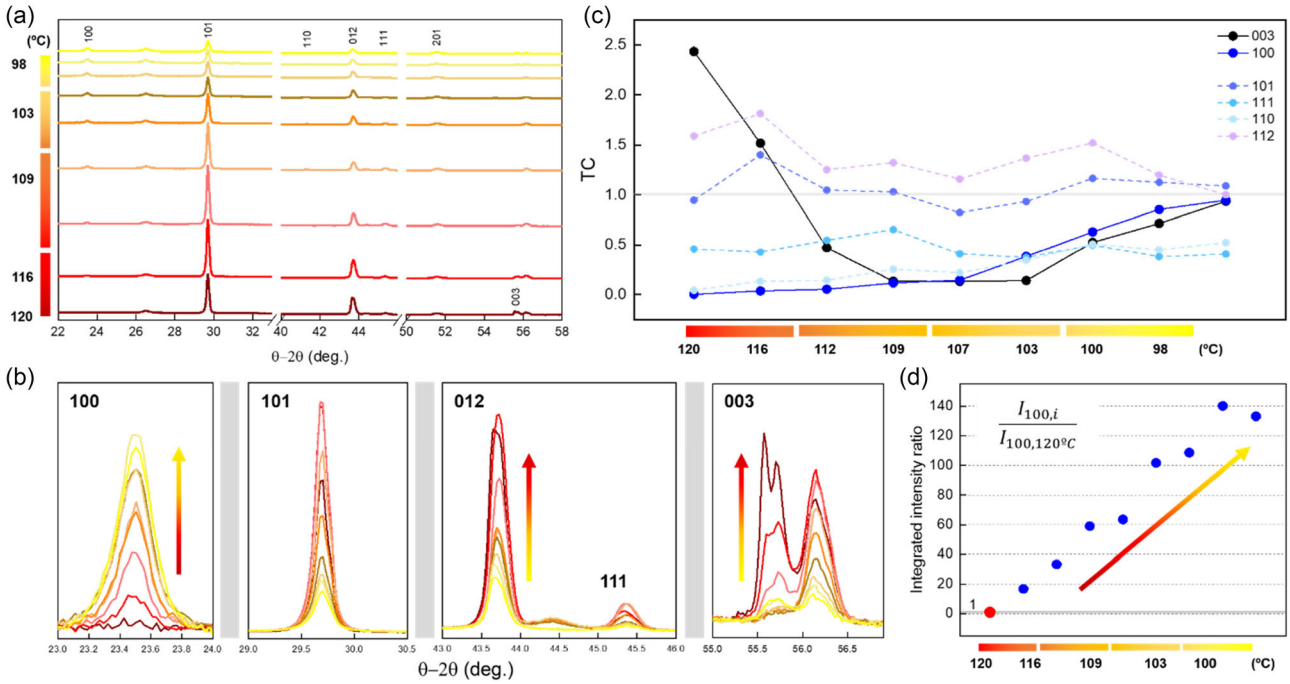

Figure 2. XRD analysis of Se films deposited by VTD. a) XRD patterns of different regions of the samples subjected to different crystallization temperatures. b) Main diffraction peaks of the Se phase—adjusted intensity. c) Texture coefficients of 003, 100, 101, 111, 110, and 112 crystallographic reflections. d) Ratio of integrated peak intensities relative to the 120 °C sample. Color scheme indicates the annealing temperature of each sample, with darker red corresponding to higher temperature (125 °C), and yellow representing the lower temperature range (<100 °C).

the TCs for key reflections, including the (003) and (100) planes, while the full set of calculated values is provided in Table S2, Supporting Information.[25–28] The Se films exhibit multiple texture components, as evidenced by several TC_{hkl} exceeding 1, indicating the absence of a single dominant orientation. Nevertheless, two distinct regimes can be identified: 1) In the higher-temperature range (120–110 °C), Se films show a clear preference for vertical orientation. Specifically, TC_{003}, TC_{101}, and TC_{112} are all above 1, while TC_{100} is negligible or 0. Notably, the sample synthesized at 120 °C exhibits the strongest (003) texture, with $TC_{003} = 2.5$, while TC_{100} and TC_{110} remain minimal. As the processing temperature decreases, the (003) orientation weakens, and TC_{101} and TC_{102} exhibit modest increases; 2) In the lower-temperature range (110–100 °C), all TCs converge toward 1, suggesting a loss of any dominant texture. Otherwise, TC_{100} increases consistently with decreasing temperature, indicating that horizontally oriented growth becomes more pronounced.

To further confirm the enhanced vertical texture in the 120 °C sample, we calculated the ratio of integrated peak intensities relative to this reference. Figure 2d presents the integrated intensity ratios for the 100 reflection, normalized to the value observed in the 120 °C sample. Since identical reflections are compared, this approach allows a direct assessment of changes in phase orientation along the [100] direction (i.e., horizontal arrangement of the Se-ribbons). Strikingly, the 100 reflection in the 120 °C sample is over a hundred times less intense than in samples synthesized at <100 °C, reinforcing the conclusion that higher synthesis temperatures promote the preferred (003)-orientation, that is, growth of the Se chains perpendicular to the substrate. Additional peak intensity ratios for the 003 and other Bragg reflections are presented in Figure S2, Supporting Information, providing further evidence that the simultaneous deposition and crystallization at 120 °C yields thin films with a strong preferential (003) orientation. While informative, the ratio of integrated peak areas does not offer a direct measurement of the proportion of a specific crystallographic orientation. However, it serves as a useful comparative metric to assess the relative dominance of specific Bragg reflections, under the assumption of similar crystallinity. To evaluate the crystalline quality, coherent diffraction domain sizes were estimated using the Scherrer formula (Equation S(2), Supporting Information) based on the fitted FWHM, see Figure S3, Supporting Information. No significant variations were observed among the nine samples, with differences falling within the margin of error. This indicates that the overall crystalline quality is comparable, and therefore, the observed differences in texture and intensity ratios can be primarily attributed to variations in preferred orientation rather than differences in crystallite size.[29]

Pole figure measurements have been performed using an X-ray diffractometer equipped with a Eulerian cradle. This advanced X-ray technique allows unambiguous determination of crystallographic texture by measuring the intensity of diffracted X-rays as a function of the orientation of a specific (*hkl*) plane relative to the sample surface.[28] It maps the distribution of the chosen crystallographic direction over a spherical projection, revealing preferred domain orientations in polycrystalline films, see **Figure 3**. Consistent with the previous TC observations, we find that samples tend to lose the (003)-preferred orientation as the processing

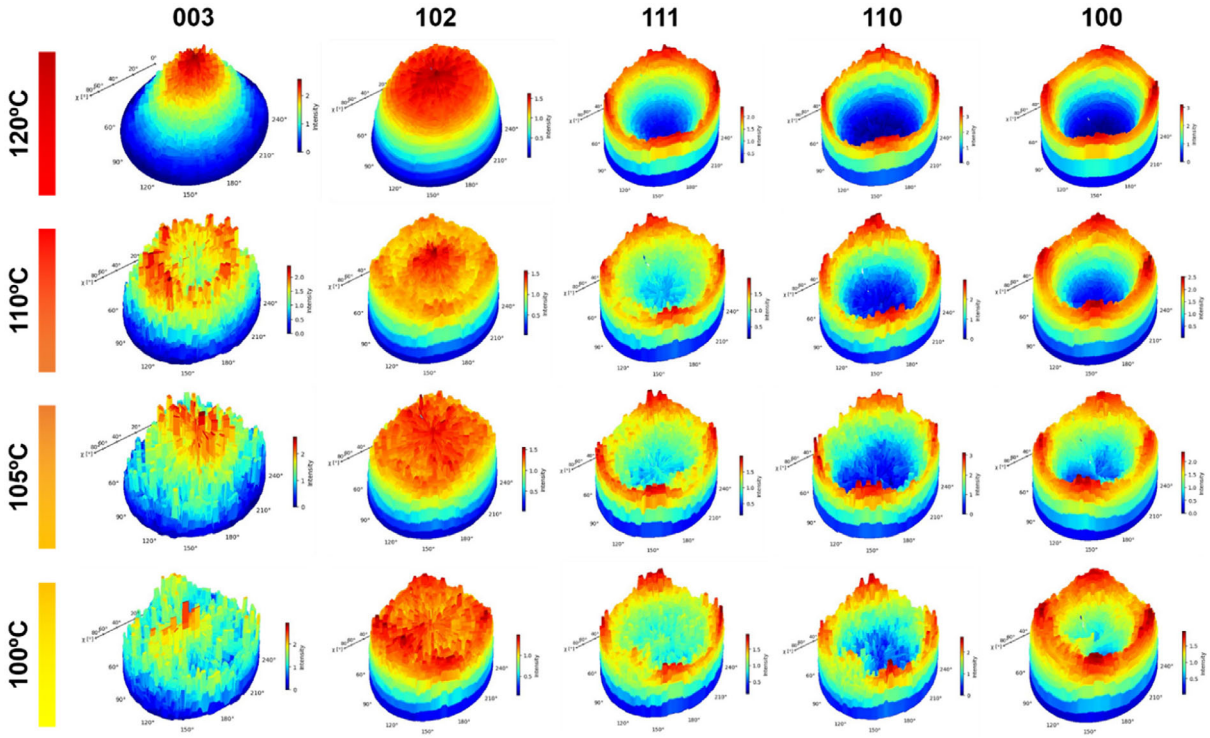

Figure 3. Pole figure measurements for selected (*hkl*) planes of Se films deposited by VTD at different substrate temperatures. Each row corresponds to a specific temperature (indicated by colon scale on the left), while columns represent different crystallographic planes.

temperature decreases, as seen by pole figures with more diffuse and uniform intensity distribution. Notably, the (003) pole figure of the sample treated at 120 °C shows a maximum intensity at $\chi = 0°$ (tilt angle), decreasing radially with increasing χ, while displaying a random azimuthal (φ) distribution. This radial symmetry indicates that (003) planes are preferentially aligned parallel to the sample surface—that is, growth is promoted in a way that the crystallographic c-axis is perpendicular to the sample surface. This is characteristic of fiber texture, where grains are randomly rotated around the c-axis, but aligned along it. In contrast, the (100) and (110) pole figures exhibit intensity maxima forming rings near $\chi \approx 80°$, suggesting that the crystallographic a and b-axes are lying in-plane. Overall, pole figure analysis reveals that texture becomes more pronounced with increasing temperature, reinforcing the (003) preferred orientation.

The morphology evolution of the various Se samples was investigated using SEM, as shown in **Figure 4**. Eight representative micrographs are presented, each corresponding to distinct regions identified in the photograph of the as-grown films, also included in Figure 4. This analysis provides valuable insight into the deposition and growth mechanism of Se, as well as the effect of temperature on film formation. First, Figure 4-1—corresponding to the region subjected to the highest temperature in the experiment (125 °C)—reveals a non-uniform morphology, with large areas where the underlying FTO substrate is exposed, indicating lack of film continuity. This inhomogeneity may result from a reduced film thickness in this region (see the thickness profile in Figure 1), or from re-evaporation of Se during deposition due to the elevated temperature. Such morphological features are generally detrimental to device performance. As the synthesis temperature decreases and film thickness increases, reaching up to 1 µm, the morphology becomes more uniform and compact, with no visible voids, and the grain sizes reaching up to 2 µm in width (Figure 4–2). It is important to note that grain size as observed in SEM images does not directly correlate with the coherent diffraction domains as obtained from XRD, which are typically smaller. Finally, at temperatures below 115 °C, a distinct morphological transition occurs. Compact layers with rounded, faceted grains give way to needle-like structures, of less than 1 µm in width, resulting in a highly roughened surface (Figure 4-5 to 8). This morphology is commonly observed in other low-dimensional chalcogenides, such as Sb chalcohalides (SbSeI, SbSI...etc.).[11] The presence of these features suggests that selenium nucleates at multiple points across the substrate, promoting anisotropic growth along the *c*-axis, and resulting in the characteristic columnar structures. Indeed, the inhomogeneous distribution and random orientation of these microcolumnar structures suggest a lack of crystallographic texture, consistent with the texture coefficient data shown in Figure 2c. On the other hand, at higher annealing temperature, these needle-like structures widen and evolve into granular features, coalescing into smoother, compact films. This progression in grain growth and coalescence aligns with the development of (003) preferred orientation.

3.2. Optical Characterization

The optical properties of the Se thin films were investigated using UV–vis transmission and reflectance spectroscopy, as well

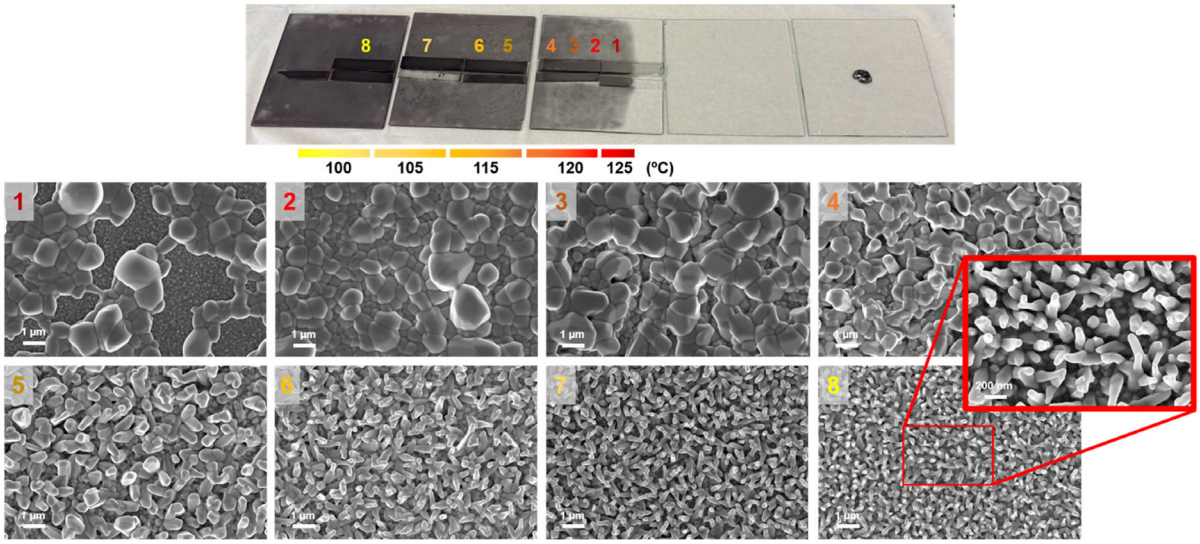

Figure 4. SEM micrographs of Se samples synthesised via the VTD method. Each numbered image corresponds to a specific position along the furnace tube, as indicated in the experimental setup photograph above.

as PDS. The absorption coefficient (α) was calculated from the internal absorbance of the films, based on thickness values obtained by X-ray fluorescence (XRF), as shown in Figure 1. For the UV–vis measurements, the internal absorbance was determined using the expression $A = 1 - T/(1-R)$, where T and R are transmittance and reflectance, respectively. In the case of PDS, the absorbance was estimated by normalizing the PDS signal to its high-energy saturation value. Subsequently, the optical bandgap (E_g) and Urbach energy (E_U) were extracted by fitting the absorption edge in both the UV–vis and PDS spectra, using a spline-based fitting model that combines Urbach-(indirect Tauc)-direct Tauc behavior (see Equation S(3), Supporting Information).[30] Notably, the inclusion of intermediate indirect Tauc region between the Urbach exponential tail and the direct band-to-band transition was necessary in order to accurately modelling the absorption edge; the full set of fitting parameters is provided in Table S3 and S4, Supporting Information. For reference, transmission, reflectance, and absorbance spectra from UV–vis measurements are shown in Figure S4, Supporting Information, while Figure S5 and S6, Supporting Information display the fitted UV–vis and PDS α spectra, including expanded caption of the absorption edge, and extracted values of *Eg* and Urbach energy.

Remarkably, PDS enables highly sensitive optical analysis in the subgap region, providing a valuable metric for assessing material quality. Elevated PDS signals in the subgap range typically indicate the presence of defect states or structural disorder, which give rise to optical transitions at energies below the bandgap. These features are commonly attributed to the presence of localized states associated with an exponentially decaying tail of the density of states (referred to as Urbach tails), characterized by the Urbach energy, E_U.[10,31,32] A larger E_U reflects increased band tailing and is generally associated with higher structural disorder and the presence of sub-bandgap states which can act as nonradiative recombination centers. This, in turn, can reduce carrier lifetimes and contribute to a larger open-circuit voltage (V_{OC}) deficit. In contrast, lower E_U values are indicative of sharper absorption edges and improved structural order, properties that are critical for high PV efficiency, specially under low-light conditions. In the present study, the PDS spectra exhibit sharp absorption fronts with minimal subgap absorption, often approaching the noise limit of the measurement. However, within the range of 1.0–1.5 eV, notable variation in the subgap absorbance is observed across samples, see **Figure 5**a. Specifically, samples synthesised at higher temperatures exhibit the lowest subgap absorption, whereas those prepared at lower temperatures show a pronounced increase in subgap signal, including a characteristic postedge bump (highlighted in the yellow spectra in Figure 5a). This trend is reflected in the corresponding E_U values shown in Figure 5b. Samples annealed in the 120–110 °C range exhibit remarkably low E_U, consistently below 40 meV (for comparison, in well-optimized chalcogenide materials such as CIGS, values between 20 and 30 meV are considered excellent).[33] In contrast, samples processed below 110 °C show a substantial increase in E_U, reaching values of 45–50 meV. This transition mirrors the two distinct textural regimes observed in Figure 2, suggesting that an improved 003-preferred crystalline orientation contributes directly to reducing the Urbach energy and subgap absorption. Additionally, Figure 5b includes the extracted width of the transition region $E_1 - E_2$, which spans from the upper limit of the exponential Urbach tail (E_1) to the onset of the direct Tauc behavior (E_2). This intermediate region was fitted using an indirect Tauc spline, from which an apparent "indirect" gap was obtained. In materials exhibiting a clearly direct E_g, the origin of this apparent indirect gap—particularly evident in PDS, but also observed in optical measurements—may be related to structural disorder within the crystal. It is worth noting that the indirect Tauc model corresponds to the original formulation developed to describe absorption in amorphous semiconductors.[34] Within this framework, both the Urbach tail and the width of the "indirect transition" $E_1 - E_2$ could be associated with localized states within the Se bandgap. The data appear to

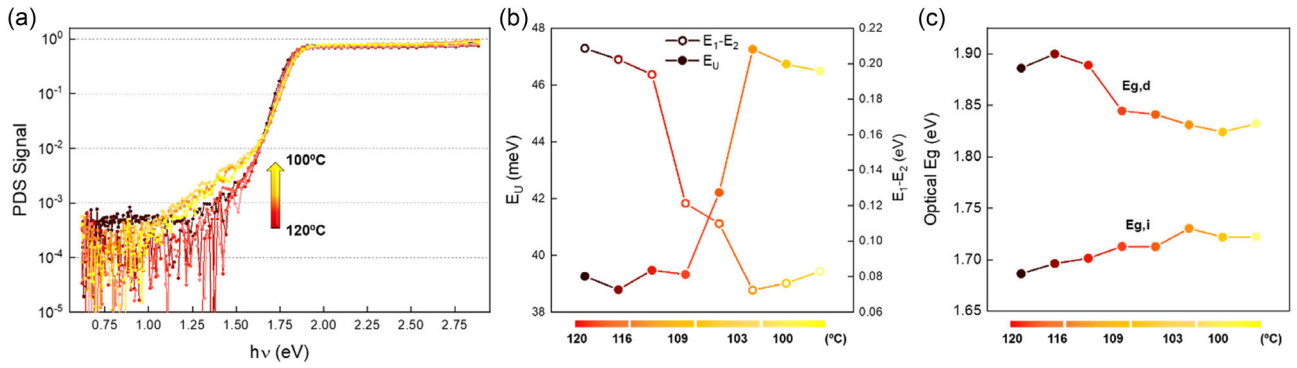

Figure 5. a) Photothermal deflection spectroscopy (PDS) spectra of eight Se samples synthesized by the VTD method. b) Urbach energy (E_U) and width of the transition region (E_1–E_2) obtained from the PDS spectra. c) Direct and indirect bandgaps (E_g) measured by optical spectroscopy and PDS, respectively.

suggest a redistribution between these two regions of localized states as the temperature decreases.

Moreover, the direct and "indirect" bandgaps were extracted from both UV–vis spectroscopy and PDS. While both techniques yielded consistent results, the optical spectra provided a better fit for the direct bandgap (Eg, d), whilst the most reliable estimate for the "indirect" bandgap (E_g, i) was obtained from the PDS data (see corresponding fits in Figure S5 and S6, Supporting Information). The evolution of the extracted Eg values as a function of annealing temperature is shown in Figure 5c. Interestingly, the direct bandgap (E_g, d) exhibits a two-regime behavior as well, with samples annealed in the 120–110 °C range showing a consistent Eg of ≈1.90 eV, while those processed at lower temperatures display a reduced bandgap, decreasing to ≈1.85 eV. Interestingly, the PDS spectra exhibiting a better fit for the indirect bandgap model, with values around 1.70 eV, may reflect the presence of defect-assisted transitions that could contribute to nonradiative recombination and V_{OC} losses, pointing to a possible limitation for Se solar cells.[35]

3.3. Solar Cell Characterization

To assess the impact of structural, morphological, and optical properties on device performance, optoelectronic characterization was carried out through JV measurements under both AM1.5 G and IPV illumination conditions. **Figures 6**a–d present the key performance parameters extracted from 30 solar cells, each fabricated at a different position along the furnace tube (see experimental configuration in Figure 1). The color scheme reflects annealing temperature; darker red indicates higher temperatures (125–120 °C), and yellow corresponds to lower temperatures, further from the Se source. As expected, the highest efficiencies were achieved in the region near 120 °C, where the 003 texture is more pronounced. Power conversion efficiency (PCE) increases from ≈3.5% at 125 °C to a maximum of 4.2% at 120 °C, then declines steadily to just over 0.5% for the lowest-performing cells, following a clear temperature-dependent downward trend. Remarkably though, a noticeable drop in performance occurs in the transition region between ≈120 and ≈112 °C, coinciding with a change in substrate, together with loss of preferential 003 texture, and the appearance of needle-like morphology (see Figure 2c and 4). These observations suggest a strong link between structural degradation and reduced performance. Other PV parameters show similar temperature-dependent trends. While the open-circuit voltage (V_{OC}) remains relatively stable between 650 and 700 mV, both short-circuit current density (J_{SC}), and fill factor (FF) decrease significantly at lower temperatures. In particular, FF closely mirrors the behavior of PCE, likely due to increased charge transport losses or enhanced non-radiative recombination. Dark J–V analysis (see Figure S7, Supporting Information) shows that both series resistance (R_S) and shunt resistance (R_{SH}) remain relatively unchanged, ruling out R_S as the limiting factor below 110 °C. Notably, the average R_{SH} ($\approx 10^6\ \Omega\,cm^2$) ranks among the highest reported for Se solar cells, underscoring the VTD method's capability to suppress shunting pathways.[14,36] Additional insight was obtained by studying the saturation current density (J_0) and ideality factor (n), shown in Figure 6e,f. Both exhibit a U-shaped dependence on annealing temperature; high values at 125–120 °C ($n \approx 2.5$ and $J_0 \approx 10^{-7}\,A\,cm^{-2}$), drop sharply in the optimal range of 120–112 °C ($n \approx 1.6$ and $J_0 \approx 10^{-10}\,A\,cm^{-2}$), to increase again at lower temperature, stabilizing around $n \approx 2.0$ and $J_0 \approx 10^{-9}\,A\,cm^{-2}$. These trends align very well with the evolution of PCE, FF, and (003)-texture, suggesting that improved vertical orientation reduces recombination. Given that J_0 is indicative of recombination losses,[37] and n values between 1.5 and 2.0 are typically associated with Shockley–Read–Hall (SRH) recombination,[38] it is likely that non-radiative recombination dominates at lower annealing temperatures. While further evidence is needed, these results strongly support the role of (003)-preferred orientation in enhancing Se solar cell performance.

Hence, here we establish a clear correlation between (003)-preferred crystallographic orientation and PV performance. As shown in Figure 6g, both the PCE and FF increase consistently with the texture coefficient TC_{003}, exhibiting an approximately linear trend when TC_{003} exceeds 0.5. In contrast, the opposite orientation—associated with (100) planes, indicative of horizontal growth—shows a markedly different behavior, see Figure 6h. As TC_{100} increases above 0.1, both PCE and FF

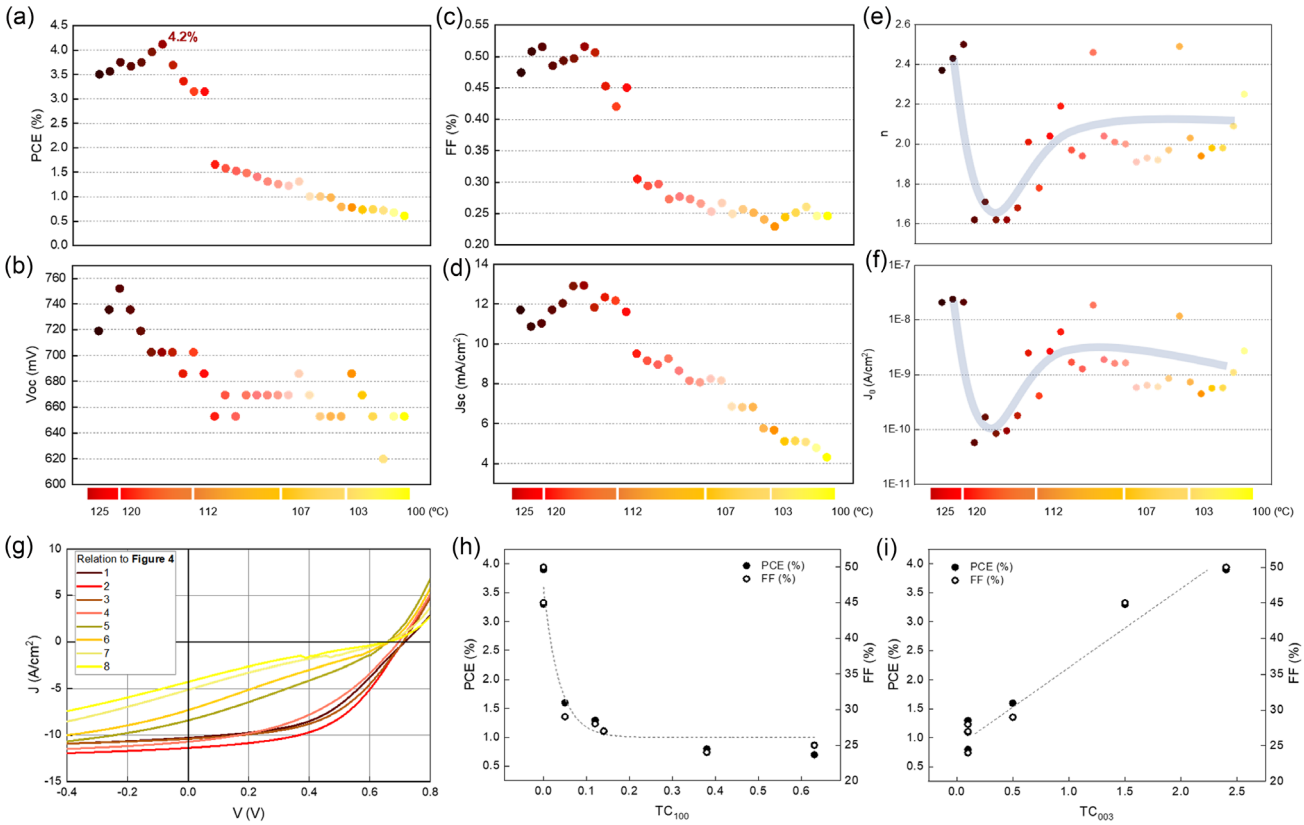

Figure 6. Optoelectronic parameters extracted from *J–V* and dark *J–V* curves of Se solar cells prepared under annealing temperatures—color bar indicates temperature. a) PCE, b) V_{OC}, c) FF, d) J_{SC}, e) ideality factor n, and f) saturation current. g) *J–V* curves of 8 selected cells corresponding to the regions shown in Figure 4. h) PCE and FF as function of texture coefficient TC_{003}, i) PCE and FF as function of TC_{100}—TC obtained from XRD analysis, see Figure 2.

decrease sharply, with efficiencies dropping from 4 to below 1%, suggesting an exponential decline in the performance. V_{OC} and J_{SC} exhibit similar trends, as shown in Figure S8, Supporting Information. Collectively, these findings highlight the strong influence of crystallographic texture on device behavior; vertical alignment along the [001] direction promotes a progressive enhancement in optoelectronic properties, whereas horizontal [100] growth leads to a rapid performance degradation.

The optoelectronic properties of the 30 Se solar cells were further investigated by external quantum efficiency (EQE) measurements (see Figure S9, Supporting Information). Overall, the EQE spectra exhibit good performance across the set of devices. Most samples, particularly those synthesised at the optimal temperatures around 120 °C, show EQE values exceeding 75% that remain stable over a broad spectral range from 400 to 550 nm. Interestingly, in the short-wavelength region, all samples maintain high EQE values in 70–75% range. However, in the long-wavelength range, EQE gradually decreases with the decreasing temperature. As a result, the overall shape of the spectrum evolves from a square-like profile towards a more trapezoidal form, with EQE declining nearly linearly between 400 and 600 nm. This behavior supports the hypothesis that Se layers synthesised at lower temperatures suffer from increased nonradiative recombination.[27,39] The bandgap has also been estimated from the absolute minimum of the first derivative of EQE spectra in the absorption edge region (600–700 nm).[40] The resulting bandgap of 2.0 eV remains constant across all 30 solar cells (see "Derivative EQE" in Figure S9a, Supporting Information), confirming that all the films are crystalline and exhibit comparable structural quality, regardless of the annealing temperature. Since crystallinity remains consistent across the whole sample set, we can rule out loss of crystallinity as the origin for the variations in PV performance, strongly suggesting that differences in crystallographic texture are the primary factor influencing the optoelectronic behavior.

Although Se has demonstrated notable improvements in PV performance over a relatively short time, its intrinsic bandgap of 1.9–2.0 eV makes it less suitable for single-junction devices compared to dominant technologies such as c-Si, CIGS, or CdTe. However, this relatively wide bandgap makes it particularly well-suited for emerging applications, including semitransparent solar cells for building-integrated PV, as top absorber in tandem cells (e.g., with c-Si), and especially for IPV.[41,42] Its bandgap aligns well with the emission spectra of common artificial light sources, such as LEDs and fluorescent lamps. This potential was already suggested as early as in 1985 by T. Nakada and A. Kunioka, who reported Se solar cell efficiencies of 11–13% under fluorescent lighting, well before

IPV was formally recognized as a field.[4] To explore this application further, we measured the *J–V* characteristics of six Se solar cells under indoor lighting, with each fabricated at a different position in the VTD tube. **Figure 7** presents color maps of the key parameters for the six representative cells as a function of incident power and color temperature. The aim of this experiment is to study IPV resilience and performance of Se solar cells across distinct conditions, without focusing on specific application scenarios, thereby facilitating comparative analysis and discussion.

The results show that J_{SC} is very sensitive to incident light intensity, decreasing significantly as power is reduced from 2500 to 500 μW cm^{-2}. In contrast, other parameters (particularly FF) exhibit a strong resilience to changing conditions. Notably, samples synthesised at 125–115 °C show minimal variation in FF across all conditions, and PCE and FF trends under IPV conditions closely mirror those under AM1.5 G, peaking at ≈10% near 120 °C, and declining at lower temperatures. To quantify this stability, resilience factors were calculated for PCE, FF, and V_{OC} (Equation S(4), Supporting Information), see **Figure 8**. A factor near 1 denotes strong stability across varying illumination. Most devices show resilience factors close to 1, with only slight increases (up to ≈1.5) in the 125 °C samples. FF remains particularly stable for the highest-performing cells (PCE > 7%), while samples synthesised at lower temperatures exhibit increased variability. These findings reinforce a central conclusion of this study: Se solar cells show significantly improved and stable performance (under both AM1.5 G and indoor conditions) when

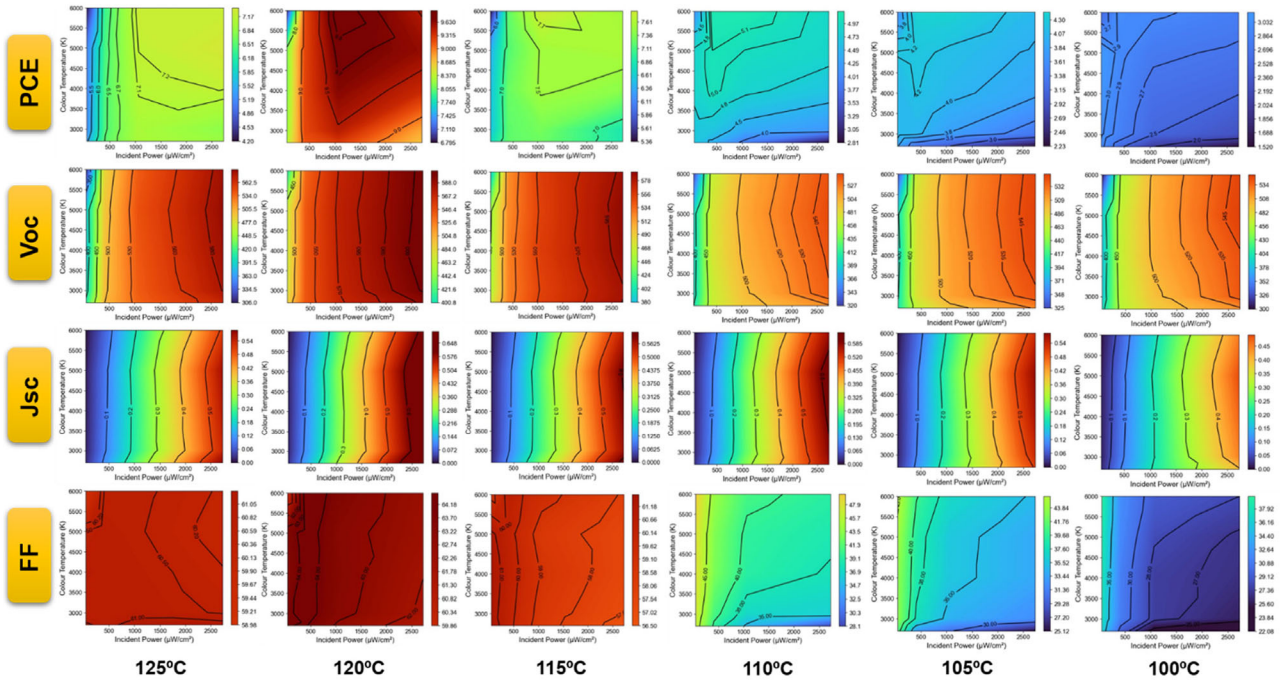

Figure 7. Filled contour plots of PV parameters for the Se devices across a range of indoor lighting conditions, showing the effects of varying incident power and color temperature on PCE (%), V_{OC} (mV), J_{SC} (mA/cm^2), and FF (%). See the complete *J–V* curves in Figure S10, Supporting Information.

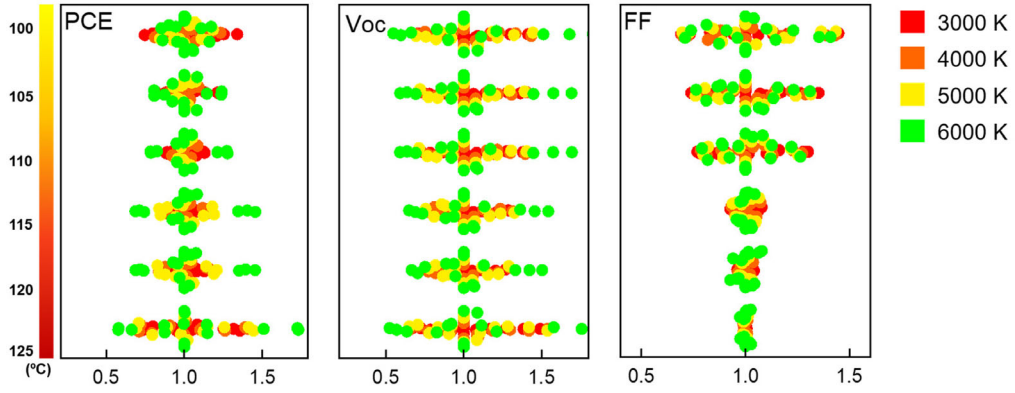

Figure 8. Resilience factors obtained from PCE, V_{OC}, and FF.

they possess a strong (003) crystallographic texture, compact morphology, and reduced nonradiative recombination. Together, these features support efficient charge transport and device robustness, positioning Se as a strong candidate for next-generation indoor photovoltaic technologies.

4. Conclusions

This work presents an innovative application of a VTD method for fabricating high-quality Se thin films at exceptionally low temperatures, opening the door to enabling compatibility with flexible and temperature-sensitive substrates, and allowing the development of comprehensive combinatorial analyses. Most importantly, we demonstrate a direct correlation between enhanced 003 crystallographic texture and improved electrical and optoelectronic properties, including reduced Urbach energy and increased performance. Texture has been determined using 3 different diffraction-based metrics; texture coefficient (TC), ratio of integrated intensities, and pole figure analysis. Devices with strong (003) orientation—that is, preferred orientation of (003) lattice planes parallel to the thin film surface—achieve over 4% efficiency under AM1.5 G and up to 10% under indoor lighting, while also showing excellent resilience across varying light intensities. These findings establish VTD as a viable route for Se processing and confirm that (003)-preferred orientation is a key element in driving the structural quality and optoelectronic performance of Se solar cells.

Supporting Information

Supporting Information is available from the Wiley Online Library or from the author.

Acknowledgements

This research has received funding from the European Union H2020 Framework Program under the SENSATE project: Low-dimensional semiconductors for optically tuneable solar harvesters (grant agreement number 866018), Renew-PV European COST action (CA21148), and Maria de Maeztu Units of Excellence Program (CEX2023-001300-M), funded by MICIN (Spanish Ministry of Science, Innovation and Universities). I.C., A.P.R., and M.P. acknowledge financial support from the Inno-PV project (PID2022-140226OB-C31, PID2022-140226OB-C32), funded by MCIN/AEI/10.13039/501100 011033/FEDER, UE. E.S. acknowledges financial support from the CURIO-CITY project (PID2023-148976OB-C41), funded by MICIN. A.P.R. and A.J.-A. acknowledge the project ENPOWER (PCI2024-155100-2, PCI2024-155054-2) from CETP-Partnership Program 2023, funded by MCIN/AEI/10.1303 9/501100011033/FEDER, UE., M.P., and A.T. acknowledge financial support from the SELECTRON project (CNS2023-14817), funded by MCIN/AEI/10.13039/501100011033/NextGenerationEU/PRTR. Z.J. is grateful to the MICINN Ramon y Cajal program (RYC2021-033239-I). E.S. acknowledges the ICREA Academia program.

Conflict of Interest

The authors declare no conflict of interest.

Data Availability Statement

The data that support the findings of this study are available from the corresponding author upon reasonable request.

Keywords

crystallographic textures, indoor photovoltaics, photovoltaics, selenium, vapor transport desposition

Received: May 11, 2025
Revised: June 23, 2025
Published online:

[1] W. G. Adams, R. E. Day, *Proc. R. Soc. London* **1877**, *25*, 171.
[2] C. E. Fritts, *Am. J. Sci.* **1883**, *3*, 465.
[3] D. M. Chapin, C. S. Fuller, G. L. Pearson, *J. Appl. Phys.* **1954**, *25*, 676.
[4] T. Nakada, A. Kunioka, *Jpn J. Appl. Phys.* **1985**, *24*, 536.
[5] I. Hadar, T. B. Song, W. Ke, M.G. Kanatzidis, *Adv. Energy Mater.* **2019**, *9*, 1802766.
[6] D. M. Bishop, T. Todorov, Y. Seog Lee, O. Gunawan, R. Haight in *2017 IEEE 44th Photovoltaic Specialist Conference (PVSC), Washington DC (USA)*, IEEE Press **2017**.
[7] Y. Gong, A. J. Arguijo, I. Caño, R. Scaffidi, C. Malerba, M. Valentini, D. Payno, A. Navarro-Güell, O. Segura-Blanch, D. Flandre, B. Vermang, A. Perez-Rodriguez, S. Giraldo, M. Placidi, Z. J. Li-Kao, E. Saucedo, *Solar RRL* **2025**, *9*, 2400756.
[8] B. Yan, X. Liu, W. Lu, M. Feng, H. J. Yan, Z. Li, S. Liu, C. Wang, J. S. Hu, D. J. Xue, *Science Advances* **2022**, *8*, 9923.
[9] W. Lu, M. Feng, Z. Li, B. Yan, S. Wang, X. Wen, X. An, S. Liu, J. S. Hu, D. J. Xue, *Joule* **2024**, *8*, 1430.
[10] I. Caño, P. Vidal-Fuentes, L. Calvo-Barrio, X. Alcobé, J. M. Asensi, S. Giraldo, Y. Sánchez, Z. Jehl, M. Placidi, J. Puigdollers, V. Izquierdo-Roca, E. Saucedo, *ACS Appl. Mater. Interfaces* **2022**, *14*, 11222.
[11] I. Caño, A. Navarro-Güell, E. Maggi, M. Barrio, J. Lluís Tamarit, S. Svatek, E. Antolín, S. Yan, E. Barrena, B. Galiana, M. Placidi, J. Puigdollers, E. Saucedo, *J. Mater. Chem. A Mater.* **2023**, *11*, 17616.
[12] Y. Zhou, L. Wang, S. Chen, S. Qin, X. Liu, J. Chen, D. J. Xue, M. Luo, Y. Cao, Y. Cheng, E. H. Sargent, J. Tang, *Nat. Photonics* **2015**, *9*, 409.
[13] C. Chen, D. C. Bobela, Y. Yang, S. Lu, K. Zeng, C. Ge, B. Yang, L. Gao, Y. Zhao, M. C. Beard, J. Tang, *Front. Optoelectron.* **2017**, *10*, 18.
[14] Q. Liu, X. Wang, Z. Li, W. Lu, X. Wen, X. An, M. Feng, H. J. Yan, J. S. Hu, D. J. Xue, *Adv. Mater.* **2024**, *37*, 2410835.
[15] W. Lu, Z. Li, M. Feng, J. Wei, X. Wen, X. An, Z. Wei, Y. Lin, J. S. Hu, D. J. Xue, *Angew. Chem. Int. Ed.* **2024**, *64*, 202413429.
[16] X. An, Z. Li, X. Wang, W. Lu, X. Wen, M. Feng, Q. Liu, Z. Wei, J. S. Hu, D. J. Xue, *Angew. Chem. Int. Ed.* **2025**, *64*, 202505297.
[17] Z. Wei, W. Lu, Z. Li, M. Feng, B. Yan, J. S. Hu, D. J. Xue, *J. Mater. Chem. A Mater.* **2023**, *11*, 23837.
[18] T. K. Todorov, S. Singh, D. M. Bishop, O. Gunawan, Y. S. Lee, T. S. Gershon, K. W. Brew, P. D. Antunez, R. Haight, *Nat. Commun.* **2017**, *8*, 682.
[19] R. Kondrotas, J. Zhang, C. Wang, J. Tang, *Solar Energy Mater. Solar Cells* **2019**, *199*, 16.
[20] X. Wen, C. Chen, S. Lu, K. Li, R. Kondrotas, Y. Zhao, W. Chen, L. Gao, C. Wang, J. Zhang, G. Niu, J. Tang, *Nat. Commun.* **2018**, *9*, 2179.
[21] E. Filippo, D. Manno, A. Serra, *Cryst. Growth Des.* **2010**, *10*, 4890.
[22] M. Salado, D. Payno, S. Ahmad, *Sustainable Energy Fuels* **2022**, *6*, 2264.

[23] J. Rodríguez-Carvajal, T. Roisnel, J. Gonzales-Platas, *FullProf Suite*, Institut Laue-Langevin (ILL), Grenoble (France) **2005**.
[24] M. Placidi, A. Torrens, Z. J. Li-Kao, A. Lopez-Garcia, O. Segura, Y. Gong, A. J. Arguijo, I. Caño, S. Giraldo, E. Saucedo, G. Alvarez, Y. Sanchez, N. Spalatu, I. Oja, E. Artegiani, A. Romeo, R. Scaffidi, A. P. Rodriguez, *Solar RRL* **2025**, *9*, 2500030.
[25] Z. Lia, X. Chena, H. Zhu, J. Chena, Y. Guoa, C. Zhanga, W. Zhanga, X. Niua, Y. Mai, *Solar Energy Mater. Solar Cells* **2017**, *161*, 190.
[26] D. Lee, J. Y. Cho, J. Heo, *Solar Energy* **2018**, *173*, 1073.
[27] I. Cano, P. V. Fuentes, A. G. Medaille, Z. Jehl, A. Jiménez-Arguijo, M. Guc, V. Izquierdo-Roca, C. Malerba, M. Valentini, M. Jiménez-Guerra, M. Placidi, J. Puigdollers, E. Saucedo, *Solar Energy Mater. Solar Cells* **2023**, *251*, 112150.
[28] R. Krautmann, N. Spalatu, R. Gunder, D. Abou-Ras, T. Unold, S. Schorr, M. Krunks, I. Oja Acik, *Solar Energy* **2021**, *225*, 494.
[29] A. L. Patterson, *Review* **1939**, *56*.
[30] A. J. Lopez-Garcia, C. Voz, J. M. Asensi, J. Puigdollers, V. I. Roca, A. Pérez-Rodríguez, *Solar RRL* **2023**, *7*, 2200928.
[31] W. B. Jackson, N. M. Amer, A. C. Boccara, D. Fournier, *Appl. Opt.* **1981**, *20*, 1333.
[32] A. C. Boccara, W. Jackson, N. M. Amer, D. Fournier, *Opt. Lett.* **1981**, *6*, 51.
[33] J. Chantana, Y. Kawano, T. Nishimura, A. Mavlonov, T. Minemoto, *Solar Energy Mater. Solar Cells* **2020**, *210*, 110502.
[34] J. Tauc, *Optical Properties of Solids*, Springer US, Boston, MA **1969**, pp. 123–136.
[35] R. Nielsen, T. H. Youngman, H. Moustafa, S. Levcenco, H. Hempel, A. Crovetto, T. Olsen, O. Hansen, I. Chorkendorff, T. Unold, P. C. K. Vesborg, *J. Mater. Chem. A Mater.* **2022**, *10*, 24199.
[36] W. Liu, F. Yu, W. Fan, W. S. Li, Q. Zhang, *Small* **2021**, *17*.
[37] A. Cuevas, *Energy Proc.* **2014**, *55*, 53.
[38] D. Abou-Ras, T. Kirchartz, U. Rau *Advanced Characterization Techniques for Thin Film Solar Cells*, Second Edition. Advanced Characterization Techniques For Thin Film Solar Cells, 2nd ed., vol. *1–2*, Wiley, Weinheim (Germany) **2016**.
[39] Y. Sun, K. H. Montgomery, X. Wang, S. Tomasulo, M. L. Lee, P. Bermel, 2015 IEEE 42nd Photovoltaic Specialist Conf.(PVSC), New Orleans (USA) **2015**, https://doi.org/10.1109/PVSC.2015.7356074.
[40] R. Carron, C. Andres, E. Avancini, T. Feurer, S. Nishiwaki, S. Pisoni, F. Fu, M. Lingg, Y. E. Romanyuk, S. Buecheler, A. N. Tiwari, *Thin Solid Films* **2019**, *669*, 482.
[41] R. Nielsen, A. Crovetto, A. Assar, O. Hansen, I. Chorkendorff, P. C. K. Vesborg, *PRX Energy* **2024**, *3*, 013013.
[42] T. H. Youngman, R. Nielsen, A. Crovetto, B. Seger, O. Hansen, I. Chorkendorff, P. C. K. Vesborg, *Solar RRL* **2021**, *5*, 2100111.